

RESEARCH

Open Access



# Dual-labeled anti-GD2 targeted probe for intraoperative molecular imaging of neuroblastoma

Lauren Taylor Rosenblum<sup>1†</sup>, ReidAnn E. Sever<sup>2†</sup>, Ryan Gilbert<sup>3</sup>, David Guerrero<sup>3</sup>, Sarah R. Vincze<sup>2</sup>, Dominic M. Menendez<sup>4</sup>, Peggy A. Birikorang<sup>4</sup>, Mikayla R. Rodgers<sup>4</sup>, Ambika Parmar Jaswal<sup>2</sup>, Alexander C. Vanover<sup>4</sup>, Joseph D. Latoche<sup>5</sup>, Angel G. Cortez<sup>5</sup>, Kathryn E. Day<sup>5</sup>, Lesley M. Foley<sup>5</sup>, Chaim T. Sneiderman<sup>2</sup>, Itay Raphael<sup>2</sup>, T. Kevin Hitchens<sup>5</sup>, Jessie R. Nedrow<sup>5</sup>, Gary Kohanbash<sup>2,6\*†</sup>, W. Barry Edwards<sup>4†</sup> and Marcus M. Malek<sup>1,7\*†</sup> 

## Abstract

**Background** Surgical resection is integral for the treatment of neuroblastoma, the most common extracranial solid malignancy in children. Safely locating and resecting primary tumor and remote deposits of disease remains a significant challenge, resulting in high rates of complications and incomplete surgery, worsening outcomes. Intraoperative molecular imaging (IMI) uses targeted radioactive or fluorescent tracers to identify and visualize tumors intraoperatively. GD2 was selected as an IMI target, as it is highly overexpressed in neuroblastoma and minimally expressed in normal tissue.

**Methods** GD2 expression in neuroblastoma cell lines was measured by flow cytometry. DTPA and IRDye<sup>®</sup> 800CW were conjugated to anti-GD2 antibody to generate DTPA- $\alpha$ GD2-IR800. Binding affinity (Kd) of the antibody and the non-radiolabeled tracer were then measured by ELISA assay. Human neuroblastoma SK-N-BE(2) cells were surgically injected into the left adrenal gland of 3.5-5-week-old nude mice and the orthotopic xenograft tumors grew for 5 weeks. <sup>111</sup>In- $\alpha$ GD2-IR800 or isotope control tracer was administered via tail vein injection. After 4 and 6 days, mice were euthanized and gamma and fluorescence biodistributions were measured using a gamma counter and ImageJ analysis of acquired SPY-PHI fluorescence images of resected organs (including tumor, contralateral adrenal, kidneys, liver, muscle, blood, and others). Organ uptake was compared by one-way ANOVA (with a separate analysis for each tracer/day combination), and if significant, Sidak's multiple comparison test was used to compare the uptake of each organ to the tumor. Handheld tools were also used to detect and visualize tumor in situ, and to assess for residual disease following non-guided resection.

<sup>†</sup>Lauren Taylor Rosenblum and ReidAnn E. Sever co-first authors.

<sup>†</sup>Gary Kohanbash, W. Barry Edwards and Marcus M. Malek co-senior authors.

\*Correspondence:

Gary Kohanbash  
gary.kohanbash2@chp.edu  
Marcus M. Malek  
marcus.malek@chp.edu

Full list of author information is available at the end of the article



**Results**  $^{111}\text{In}$ - $\alpha\text{GD2-IR800}$  was successfully synthesized with 0.75–2.0 DTPA and 2–3 IRDye® 800CW per antibody and retained adequate antigen-binding ( $K_d = 2.39$  nM for  $\alpha\text{GD2}$  vs. 21.31 nM for DTPA- $\alpha\text{GD2-IR800}$ ). The anti-GD2 tracer demonstrated antigen-specific uptake in mice with human neuroblastoma xenografts (gamma biodistribution tumor-to-blood ratios of 3.87 and 3.88 on days 4 and 6 with anti-GD2 tracer), while isotype control tracer did not accumulate (0.414 and 0.514 on days 4 and 6). Probe accumulation in xenografts was detected and visualized using widely available operative tools (Neoprobe® and SPY-PHI camera) and facilitated detection of putative residual disease in the resection cavity following unguided resection.

**Conclusions** We have developed a dual-labeled anti-GD2 antibody-based tracer that incorporates In-111 and IRDye® 800CW for radio- and fluorescence-guided surgery, respectively. The tracer adequately binds to GD2, specifically accumulates in GD2-expressing xenograft tumors, and enables tumor visualization with a hand-held NIR camera. These results encourage the development of  $^{111}\text{In}$ - $\alpha\text{GD2-IR800}$  for future use in children with neuroblastoma, with the goal of improving patient safety, completeness of resection, and overall patient outcomes.

**Keywords** Intraoperative molecular imaging, Neuroblastoma, GD2, Radio-guided surgery, Fluorescence guided surgery, Monoclonal antibody

## Background

Neuroblastoma (NB) is the most common extracranial solid malignancy in children and accounts for 15% of pediatric cancer-related deaths [1]. Over 30% of NB patients have high-risk disease, which is associated with a 5-year survival of only 40–50% [2]. These poor outcomes are observed despite intense, multimodal therapy that includes surgery, high-dose chemotherapy, radiotherapy, autologous stem cell transplantation, and immunotherapy [3–5]. Tumor encasement of critical neurovascular structures, unclear tumor margins, and remote lymph node disease present particularly significant challenges for surgeons attempting safe and complete macroscopic excision of NB. In fact, up to 50% of patients experience significant surgery-related complications such as unplanned nephrectomies, Horner syndrome, pleural effusions, significant blood loss, or even death [6, 7]. In addition, up to 30% undergo inadequate surgery (defined as either less than 90% resection or less than complete macroscopic resection), which is associated with increased cumulative incidence of local progression and decreased event-free survival [6–8]. The challenge of safely separating cancer from critical structures that are encased in tumor and related attempts to avoid complications could also contribute to incomplete resection. Innovations to improve disease localization and clarify tumor margins intraoperatively should lead to safer operations with more complete resections, which in turn would lead to improved patient outcomes.

Approaches for aiding surgeons in the resection of cancer, such as radio-guided surgery (RGS) and fluorescence-guided surgery (FGS), have been developed over several decades and provide intraoperative surgical guidance for a number of tumors, though they have had limited translation for NB surgery. RGS utilizes gamma emissions from radioisotopes to localize regions of interest and is commonly used for sentinel lymph node biopsy

in melanoma and breast cancer [9, 10]. This technique relies on the passive accumulation of radiotracer, but receptor targeted gamma-emitting probes are now being developed, including  $^{111}\text{In}$ -labeled antibodies targeting prostate, colorectal, renal cell carcinoma, and ovarian cancers [11]. While gamma decay is detectable through several centimeters of tissue, there are no visual cues to distinguish the lesion from adjacent tissue, so it is less useful for detecting surgical margins.

In contrast, FGS provides real-time visualization of lesions through a few millimeters of tissue. Initial FGS techniques also relied on passive accumulation of tracers, such as using indocyanine green (ICG) to highlight biliary anatomy, though this leads to significant background fluorescence in cancer applications, most notably in areas of inflammation and in benign lesions. To address the shortcomings seen with the passive accumulation of tracers, receptor-targeted fluorescent tracers have recently been developed. For example, an FDA-approved targeted fluorescent agent, OTL38 (also known as pafolacianine or Cytalux), targets the folate receptor and was approved in 2021 and 2022 for intraoperative imaging of ovarian and lung cancers [12, 13]. Antibody-based targeted fluorescent probes, such as SGM-101, which targets carcinoembryonic antigen (CEA) on colorectal cancer, have also shown promising results in clinical trials [14–16]. Despite the utility of tumor visualization, near-infrared (NIR) fluorescent signal can only penetrate through 5–10 mm of intervening tissue [14, 15].

Dual-labeled IMI agents combine the advantages of RGS and FGS, enabling both depth of detection for identification of occult lesions (with radioactivity) and tumor margin visualization (with fluorescence). Accordingly, the development of targeted dual-labeled probes has gained enthusiasm, with several agents targeting adult tumors now in the early stages of development, including  $^{111}\text{In}$ -DTPA-labetuzumab-IRDye800 which targets

CEA for colorectal cancer,  $^{111}\text{In}$ -DTPA-bivatuzumab-IRDye800 which targets CD44 for head and neck cancer, and  $^{111}\text{In}$ -DOTA-girentuximab-IRDye800 for renal cell carcinoma [17–19]. While many of these dual-labeled tracers are promising, none could be used for to aid in surgical resection of neuroblastoma, as none have been FDA-approved nor are any designed for pediatric indications.

GD2 is a well-established tumor antigen, present on 98% of NB but minimal expression in normal tissues, and it is currently targeted by the monoclonal antibody, Dinutuximab, for standard maintenance immunotherapy for high-risk NB [5, 20–22]. In-111 decays by gamma emission with a half-life of 2.81 days, which is well-matched to the 1-to-4-week serum half-life of IgG antibodies, and it has a low energy emission enabling more specific detection than seen with higher energy counterparts [23, 24]. NIR fluorophores have less absorption by tissue and less overlap with tissue autofluorescence than visible spectrum fluorophores, enabling better tumor-to-noise signal and greater depth of visualization [25, 26]. IRDye<sup>®</sup> 800CW is a near-infrared (NIR) dye with high brightness that has shown promise when conjugated to antibodies for FGS. Tracers that incorporate it are now in clinical trials for pancreatic, breast, colorectal, and head and neck cancers (NCT02736578, NCT01972373, NCT01508572, NCT04511078). The specificity of the anti-GD2 antibody for NB, the low-energy gamma decay and half-life of In-111, and the optical properties of IRDye<sup>®</sup> 800CW make them well suited for a dual-labeled IMI agent.

Here, we demonstrate the ability of an anti-GD2 monoclonal antibody labeled with a gamma emitting radionuclide and a NIR fluorophore,  $^{111}\text{In}$ - $\alpha$ GD2-IR800, to enable IMI in an established orthotopic xenograft mouse model of neuroblastoma through antigen-specific accumulation.

## Methods

### In vitro maintenance of cell lines

NMB6 (Shou-Jiang Gao Lab for Cancer Virology, University of Pittsburgh), SK-N-BE(2) (ATCC no. CRL-2271), SK-N-AS (ATCC no. CRL-2137), SK-N-SH (ATCC no. HTB-11), SH-SY5Y (ATCC no. CRL-2266) and CHP212 (CHP tumor bank) cells were cultured in Dulbecco's Modified Eagle Medium (Cat# BW12614F; Lonza, Basel, Switzerland), supplemented with 10% heat-inactivated FBS (Cat# SH3091003; Cytiva Hyclone<sup>™</sup>, Logan, UT, USA), 100 mM sodium pyruvate (Cat# BW13-115E; Lonza, Basel, Switzerland), 1x Antibiotic-Antimycotic (Cat #15-240-062; Gibco, Grand Island, New York, USA), 55  $\mu\text{M}$  beta-mercaptoethanol (Cat# 21-985-023; Gibco), 1x MEM NEAA (Cat# 11140-050; Gibco), and 50 mg/mL Normicin (Cat# ant-nr-2; InvivoGen, San Diego, CA) and maintained in a 37 °C humidified incubator with 5%  $\text{CO}_2$ . SK-N-BE(2), SK-N-AS, SK-N-SH, and SH-SY5Y cell

lines were authenticated through genotypic analysis performed by ATCC.

### Flow cytometry and quantification of GD2 expression

Cells were detached from T-75 flasks (Cat# 430641U; Corning<sup>™</sup>, Corning, NY, USA) with 0.05% Trypsin / 0.53 mM EDTA in HBSS (Cat# MT25052CI; Corning<sup>™</sup>). A standard curve of fluorescence was created using BD Quantibright<sup>™</sup> beads with known levels of PE staining on the LSR Fortessa FACS machine (BD Biosciences, Franklin Lakes, New Jersey, USA), as described in the PE Fluorescence Quantitation Kit (Cat# 340495; BD Biosciences). Each cell line was stained with 1  $\mu\text{g}$ /1,000,000 cells PE anti-human Ganglioside GD2 (Cat# 357304; BioLegend<sup>®</sup>, San Diego, CA, USA) at 4 °C for 30 min. PE fluorescence was measured from at least 10,000 cells, then quantified with the linear regression of the generated standard curve. Data were analyzed using FlowJo Software, v10.8 (BD Biosciences).

### Tracer and isotype control synthesis and evaluation

To generate DTPA- $\alpha$ GD2-IR800 or DTPA-isotype-IR800, 1 mg of mouse IgG2a anti-GD2 (#BE0318; Bio X Cell, Lebanon, NH, USA) or mouse IgG2a isotype control (#BE0085; Bio X Cell) in PBS was added to 0.1 M sodium carbonate buffer, pH 9 (final pH 8.5–9). 25-fold molar excess of p-SCN-Bn-CHX-A'-DTPA (Macrocyclics, Plano, TX) was added (37 °C, 1 h). Excess DTPA was removed by centrifugal ultrafiltration (Pierce Protein Concentrator, 10 kDa MWCO, PBS diluent, Thermo Fisher Scientific, Waltham, MA, USA). Four-fold molar excess of IRDye<sup>®</sup> 800CW NHS ester (LI-COR, Lincoln, NE, USA) was added (final pH 8.5–9) and incubated (RT, 30 min, with shaking). After each conjugation, purification was performed with size exclusion HPLC (Agilent 1260, Bio SEC-3, PBS, 0.3 mL/min). DTPA substitution levels were calculated by comparing absorbance at 245 nm (DTPA) and 280 nm (protein), while IRDye<sup>®</sup> 800CW substitution levels were determined comparing absorbance at 700 nm (IRDye<sup>®</sup> 800CW) and 280 nm (protein with 3% from IRDye<sup>®</sup> 800CW) by UV-Vis Spectrophotometry (BioTek Epoch with a Take3 plate; Agilent, Santa Clara, CA, USA). Probes were protected from light and stored at less than 3 mg/ml until use.

DTPA- $\alpha$ GD2-IR800 or DTPA-isotype-IR800 was radiolabeled with In-111 using the Nalla et al. method for radiolabeling DTPA-conjugated proteins with minimal modifications [27]. In-111 stock was diluted into sodium citrate (500 mM; pH 6) to 1.6 ml and after 5 min, probe was added and incubated (25 °C, 30 min). Reaction progress was monitored by instant thin-layer chromatography (iTLC) developed in 50 mM sodium citrate eluent. The buffer was exchanged with DPBS (Cat# 175512F12; Lonza, Basel, Switzerland) for tail vein injections. Purity

was determined by SEC-HPLC (PBS, 3  $\mu$ m, 300 A, 4.6 $\times$ 300 mm, 0.4 mL/min; BioSec3, Agilent), and purification repeated until >95% pure.

To assess potential changes in GD2-specific binding affinity after conjugation of the dye and chelator, an ELISA was performed [28]. Briefly, ganglioside GD2 (Advanced ImmunoChemical Inc., Long Beach, CA, USA) was reconstituted (1 mg/ml) and immobilized on a microtiter plate (0.8  $\mu$ g/well). After blocking with 1% BSA, a range of concentrations of anti-GD2 or DTPA- $\alpha$ GD2-IR800 were added (2.6–333 nM), followed by HRP-conjugated goat anti-human IgG Fc (Thermo Fisher Scientific, Waltham, MA, USA), then visualized. Non-specific binding was determined with GD2 immobilization and secondary antibody only (HRP-conjugated goat anti-human IgG Fc), then total binding was corrected (by subtracting the non-specific binding) to yield specific binding, which was then fit by non-linear regression to yield the equilibrium dissociation constants (GraphPad Prism v9.4.1, Boston, MA, USA).

## In vivo studies

### Orthotopic xenograft mouse model

Animal studies were performed in accordance with the protocols approved by the Institutional Animal Care and Use Committee of the University of Pittsburgh (IACUC protocol number: 19126346). Four- to six-week-old nude mice (*Fox1<sup>tm</sup>*, strain #002019; The Jackson Laboratory, Bar Harbor, ME, USA) were maintained in a temperature-controlled animal facility at the UPMC Children's Hospital of Pittsburgh or the UPMC Hillman Cancer Center with a 12-hour light/dark cycle in cohorts of five. Animals were kept in the facility for at least two days prior to performing any procedures to minimize stress-related symptoms.

Tumors were grafted by the established adrenal gland injection method [29]. Under isoflurane anesthesia, a transverse left flank incision was made through skin, abdominal wall, and peritoneum. The left kidney and adrenal gland were gently exteriorized and maneuvered by palpation and with a cotton tip applicator. SK-N-BE(2) cells were trypsinized, washed, counted, and resuspended in PBS. One million SK-N-BE(2) human-derived neuroblastoma cells in 20  $\mu$ l of PBS were mixed with 20  $\mu$ l of Matrigel basement membrane matrix (#354234; Corning<sup>™</sup>, Corning, NY, USA), then injected into the left adrenal gland with a 30-gauge needle on a 1 ml syringe and the needle was slowly removed, with the Matrigel holding the cells largely in place. The kidney and adrenal gland were returned to the abdomen, the body wall was closed with 3–0 or 4–0 Polysorb, and the skin was closed with surgical wound clips (which were removed after 10–14 days). Mice were placed in a clean cage on a warming pad provided with easily accessible food on the cage bottom,

and monitored at least every 15 min until sternal recumbency was regained and they had fully recovered from anesthesia.

Tumor size was measured by MRI 5 weeks after tumor injection (7T/30-cm AVIII spectrometer, Bruker Biospin, Billerica, MA; 12 cm gradient set, 40 mm quadrature RF volume coil, and Paravision 6.0.1 software). A T1-weighted Intragate FLASH sequence was used (repetition time (TR)/echo time (TE)=162/2.6 ms, field of view 40 $\times$ 40 mm, acquisition matrix 256 $\times$ 256, 13 slices, slice thickness 1 mm, and 1 average). Tumor size on MRI images was measured using DSI Studios software. Euthanasia was planned for any animals that reached USDA Class D sacrifice requirements, though none did prior to planned euthanasia. All mice grew tumors and were included in the study. Mice were excluded from analysis for clear and uncorrectable data errors (multiple organs with uptake and weight more than 2 standard deviations from others in the group).

### Handheld gamma detection, fluorescence detection, and biodistribution studies

Mice were used for further experiments 3.5–5 weeks after SK-N-BE(2) injection, when tumors were approximately 0.5–1 cm large ( $n=33$  in total, including 26 for anti-GD2 tracer groups and 7 for isotype control groups). For each experiment, mice were randomly assigned to each group.

On the day of radiolabeling, <sup>111</sup>In- $\alpha$ GD2-IR800 ( $n=7$  for day 4 and  $n=7$  for day 6) or <sup>111</sup>In-isotype-IR800 ( $n=4$  for day 4 and  $n=3$  for day 6) was injected intravenously by tail vein (0.5–4.8 MBq/50  $\mu$ g in 100 $\mu$ L DPBS). Three and four days after tracer injection, gamma counts from the day 4 tracer group were measured percutaneously from the left flank (tumor), right flank, left and right hind limbs, tail, and chest using a Neoprobe<sup>®</sup> gamma decay detector (Mammotome, Cincinnati, OH, USA). Four or six days after tracer or isotype control injection, mice were euthanized for gamma biodistribution analysis. NIR imaging was performed with the SPY-PHI NIR camera (Stryker, Leesburg, VA, USA) post-laparotomy, with representative images recorded.

Personnel performing injections and biodistribution studies were not blinded as to whether probe or isotype control was administered. The indicated organs were harvested and weighed (liver piece, spleen, tumor, blood, muscle piece, femur bone piece, right adrenal, left kidney, right kidney, heart, lung, section of small intestine, and brain). Tissue-associated radioactivity was measured by gamma counter (PerkinElmer Wizard 2, model 2480; PerkinElmer, Waltham, MA, USA) and quantified as percent injected dose (corrected for In-111 decay from the dose measured at the time of injection) per gram of tissue (%ID/g). One mouse was removed from the study (in the day 6 <sup>111</sup>In- $\alpha$ GD2-IR800 gamma biodistribution group)

because of an uncorrectable data error (leading to  $n=6$  for that group).

For the optical biodistribution, additional tumors were grown ( $n=10$ ) and after 4.5 weeks,  $^{111}\text{In}$ - $\alpha\text{GD2}$ -IR800 was injected intravenously (6.3 MBq/74.6  $\mu\text{g}$  in 100 $\mu\text{L}$  DPBS). Mice were euthanized 4 or 6 days later ( $n=5$  each). Organs were harvested and placed on a minimally fluorescent black PLA printed plate, and images were acquired with the SPY-PHI camera, and saved using a NIX HDMI capture card (model USBC-CAP60, Plugable Technologies, Redmond, WA, USA) and OBS video capture software (Open Broadcaster Software, open source). To define regions of interest (ROIs) for each organ, the brightness and contrast were uniformly enhanced on each image to enable visualization of even minimally fluorescent organs. ROIs were drawn by one of the investigators (LTR) around each organ, and a background region of the PLA plate, then those ROIs were applied to the original, unenhanced image (ImageJ, NIH; Supplementary Fig. 3). The average fluorescence intensity per pixel<sup>2</sup> was quantified for each ROI on the original, unenhanced image (in arbitrary units per pixel<sup>2</sup>, or AU/p<sup>2</sup>). Average fluorescence of the background was subtracted from the mean fluorescence of each organ. The identical method was used to measure fluorescence from organs of mice given  $^{111}\text{In}$ -isotype-IR800 ( $n=4$  and 3 for each day, using the same mice as the gamma biodistribution experiment above).

To evaluate the practical use of the anti-GD2 tracer with widely available intraoperative tools, standard, non-IMI guided resection was conducted 4 days after tracer injection ( $n=2$ ). The intraoperative systems were then used to inspect for residual disease, and if identified, used to guide additional resection until no further disease could be detected.

### Tissue phantom studies

Tracer-bearing NB xenografts harvested from tumor-bearing mice for the biodistribution studies ( $n=4$ ) were implanted below 5 cm of processed tissue (Supplementary Fig. 5). Neoprobe<sup>®</sup> and SPY-PHI handheld instruments were used to measure gamma decay and fluorescence from the surface of the overlying processed tissue with the removal of 5 mm increments of tissue, until the implanted xenograft was reached.

### Image processing and statistical analysis

Images for the fluorescence biodistribution were analyzed with ImageJ (NIH). Graphs were generated and statistical analyses were performed using Prism GraphPad v10. Organ uptake (%ID/g) in the biodistribution experiments is reported as mean $\pm$ SEM. Probe accumulation within organs was compared using one-way ANOVA, and if significant, the Sidak post-hoc test was used to compare the uptake of each organ to the tumor uptake. The tracer and isotype control experiments were run separately, so one-way ANOVA was used for each.

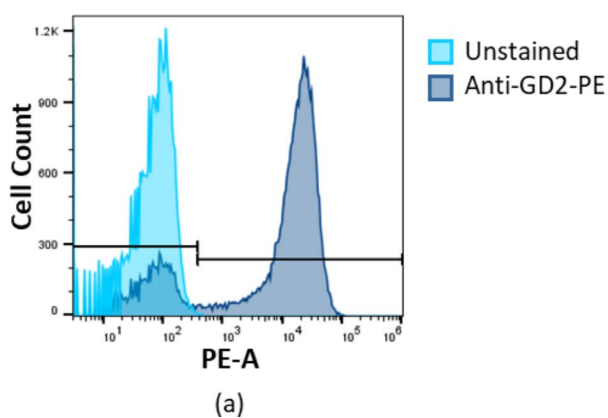
## Results

### Neuroblastoma cell lines express GD2

Among six NB cell lines evaluated, the average GD2 molecules/cell varied widely (Fig. 1). As our prior imaging of myeloid cells in tumors demonstrated successful immunoPET with  $\sim 60,000$  molecules/cell, we selected SK-N-BE(2) cells to establish xenograft models for subsequent studies, given its intermediate range among cell lines tested with an average of  $215,288 \pm 54,401$  molecules of GD2 and its wide usage in preclinical research and established in vivo growth [30, 31].

### Tracer characterization

$^{111}\text{In}$ - $\alpha\text{GD2}$ -IR800 was synthesized with high radiochemical yield (>90%) at the target molar activity (11.11 MBq/



NB Cell Line	GD2/Cell
NMB6	975,133 $\pm$ 72,434
SK-N-BE(2)	215,288 $\pm$ 54,401
SK-N-AS	154,998 $\pm$ 2,433
SH-SY5	85,672.36 $\pm$ 28,033
CHP212	13,509 $\pm$ 9,067
SH-N-SH	2,420 $\pm$ 941

**Fig. 1** Human NB cell lines express GD2. (a) FACS histogram of unstained SK-N-BE(2) cells, unlabeled (left) versus labeled with PE-bound anti-GD2. (b) Quantification of average GD2 molecules per cell in human NB cell lines

nmol). Substitution levels ranged from 0.75 to 2.0 DTPA chelators/antibody and 2–3 IRDye® 800CW dyes/antibody, as determined by UV-Vis spectra comparing absorbance at 245 nm (DTPA) and 700 nm (IRDye® 800CW) versus 280 nm (protein) (Supplementary Fig. 1). Optimization studies performed with more than 4 IRDye® 800CW/antibody showed slight precipitation of the antibody. With fewer than 4 IRDye® 800CW/antibody, no precipitation was observed on visual inspection and aggregation was not seen with SEC-HPLC (Supplementary Fig. 1). The binding affinities ( $K_d$ ) for anti-GD2 and DTPA- $\alpha$ GD2-IR800 were 2.39 nM (0.99–4.62 nM, 95% CI) and 21.31 nM (14.06–32.16 nM, 95% CI), respectively. These data support the feasibility of generating  $^{111}\text{In}$ - $\alpha$ GD2-IR800.

### Biodistribution analysis

Orthotopic SK-N-BE(2) xenografts were successfully grown in nude mice, reaching  $907.5 \pm 44.6 \text{ mm}^3$  in volume ( $13.8 \pm 0.24 \text{ mm}$  in largest dimension) after 5 weeks of growth on MRI. In several mice, the left kidney was embedded within the tumor (Supplementary Fig. 2).

Specific accumulation of  $^{111}\text{In}$ - $\alpha$ GD2-IR800 or  $^{111}\text{In}$ -isotype-IR800 in GD2-expressing neuroblastoma tumors and non-target organs was examined by gamma decay count and fluorescence biodistribution analysis. All mice tolerated tracer administration well with no noted adverse effects. On both 4 and 6 days after probe injection,  $^{111}\text{In}$ - $\alpha$ GD2-IR800 showed greater tumor accumulation than almost all other measured organs, while corresponding isotype control tracer ( $^{111}\text{In}$ -isotype-IR800) did not.

Gamma biodistribution analysis of  $^{111}\text{In}$ - $\alpha$ GD2-IR800 in NB-bearing mice 4 days after tracer injection ( $n=7$ ) demonstrated significantly higher uptake in the tumor ( $13.5 \pm 5.27\% \text{ID/g}$ ) compared to blood ( $3.49 \pm 0.75\% \text{ID/g}$ ;  $p < 0.001$ ) and muscle ( $0.45 \pm 0.06\% \text{ID/g}$ ;  $p < 0.0001$ ) (Fig. 2a), with tumor-to-background (TBR) ratios of 3.87 and 30.0, respectively. As is common with IgG-based tracers, non-specific accumulation was noted in the liver ( $10.25 \pm 1.45\% \text{ID/g}$ ;  $p = \text{ns}$ ) and the spleen ( $7.66 \pm 0.50\% \text{ID/g}$ ;  $p = \text{ns}$ ), though accumulation was greater in the tumor than all other measured organs ( $p < 0.005$ ). Similarly, six days after tracer injection ( $n=6$ ), tumor uptake ( $5.58 \pm 0.48\% \text{ID/g}$ ) was significantly higher than all other organs ( $p < 0.0001$ ) except the liver ( $7.70 \pm 0.73\% \text{ID/g}$ ,  $p < 0.01$ ), including the blood ( $1.44 \pm 0.26\% \text{ID/g}$ ) and muscle ( $0.19 \pm 0.01\% \text{ID/g}$ ) (Fig. 2a), with TBR ratios of 3.88 and 29.4, respectively.

Fluorescence biodistribution using the SPY-PHI camera and ImageJ analysis yielded similar results (Fig. 2b): On both days ( $n=5$  each), average fluorescence intensity was significantly higher in tumor ( $37.9 \pm 7.88 \text{ AU/p}^2$  on day 4 and  $16.8 \pm 4.30 \text{ AU/p}^2$  on day 6) versus all other

organs ( $p < 0.001$ , except day 4 vs. each kidney  $p < 0.01$ ). On day 4, accumulation was low in the blood ( $3.80 \pm 0.54 \text{ AU/p}^2$ ) and muscle ( $4.57 \pm 0.52 \text{ AU/p}^2$ ), with tumor-to-blood and tumor-to-muscle differences of 34.1 and 33.3 respectively. Similarly on day 6, fluorescence was low in blood ( $0.43 \pm 0.15 \text{ AU/p}^2$ ), and muscle ( $0.8 \pm 0.045 \text{ AU/p}^2$ ), with tumor-to-blood and tumor-to-muscle ratios of 16.37 and 16.0, respectively.

Isotype control ( $^{111}\text{In}$ -isotype-IR800) accumulation in tumors, however, was low both by gamma and optical biodistribution analysis ( $n=5$  for each time point). Accumulation was similar in tumor ( $1.34 \pm 0.87$  on day 4;  $1.56 \pm 0.89\% \text{ID/g}$  on day 6) and most other organs ( $p = \text{ns}$ ) and was actually significantly lower than the spleen (day 4,  $p < 0.05$ ) and the liver (both days,  $p < 0.0001$ ) (Fig. 2c). Tumor-to-blood ratios of  $^{111}\text{In}$ -isotype-IR800 were 0.414 on day 4 and 0.514 on day 6 (9.3- and 7.5-fold lower than ratios in  $^{111}\text{In}$ - $\alpha$ GD2-IR800), while tumor-to-muscle ratios were 5.88 on day 4 and 6.32 on day 6 (5.1- and 4.7-fold lower than  $^{111}\text{In}$ - $\alpha$ GD2-IR800).

Similarly, tumor brightness was quite low after injection of  $^{111}\text{In}$ -isotype-IR800 ( $5.03 \pm 1.3 \text{ AU/p}^2$  on day 4 and  $4.34 \pm 1.69 \text{ AU/p}^2$  on day 6; Fig. 2d). Four days after control tracer injection, fluorescence was still significantly higher in the tumor than the heart ( $1.24 \pm 0.06 \text{ AU/p}^2$ ;  $p < 0.001$ ), blood ( $0.521 \pm 0.06 \text{ AU/p}^2$ ;  $p < 0.0001$ ), muscle ( $0.89 \pm 0.09 \text{ AU/p}^2$ ;  $p < 0.001$ ), and adrenal gland ( $1.88 \pm 0.31 \text{ AU/p}^2$ ;  $p < 0.01$ ), but significantly lower than liver ( $15.4 \pm 1.55 \text{ AU/p}^2$ ;  $p < 0.0001$ ). Six days after control tracer injection, tumor fluorescence remained was only significantly higher than blood ( $0.59 \pm 0.20$ ;  $p < 0.05$ ) while much lower than liver ( $11.82 \pm 1.59$ ;  $p < 0.0001$ ). The tumor-to-blood difference in fluorescence was also substantially lower with the isotype control tracer (4.51 and 4.14 on days 4 and 6, versus 34.1 and 16.37 with the  $^{111}\text{In}$ - $\alpha$ GD2-IR800). A similar decrease was in the tumor-to-muscle difference was seen (4.14 and 3.84 on days 4 and 6 versus 33.3 and 16.0 with  $^{111}\text{In}$ - $\alpha$ GD2-IR800).

### Handheld clinical IMI detection systems

To evaluate tracer detection in vivo, NB-bearing mice received tail vein injections of  $^{111}\text{In}$ - $\alpha$ GD2-IR800 ( $4.8 \text{ MBq}/50 \mu\text{g}$  in  $100 \mu\text{l}$  DPBS;  $n=4$  using mice in the gamma biodistribution group). Three and four days later, gamma decay of body regions was measured percutaneously with the handheld Neoprobe®. At both time points, gamma decay signal was significantly higher in the tumor-bearing left flank than any other body region (Fig. 3a;  $p < 0.0001$ ). Following laparotomy, fluorescence was subjectively evaluated with the handheld NIR camera, demonstrating strong qualitative fluorescence of the tumor with little surrounding signal (Fig. 3c and d; Supplementary Fig. 3b and c) while minimal tumor fluorescence was observable following similar isotype control

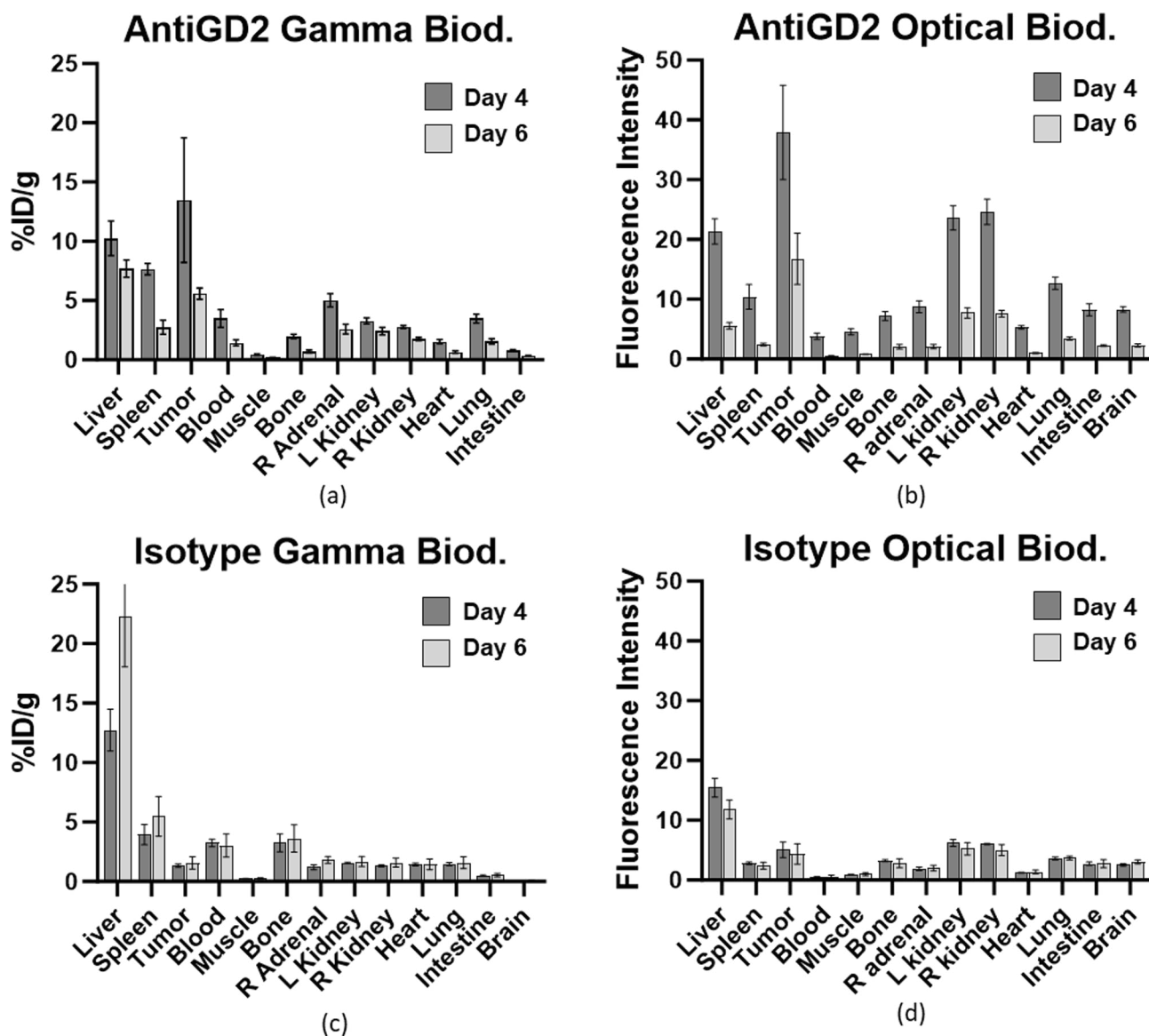


**Fig. 2**  $^{111}\text{In}$ - $\alpha\text{GD2}$ -IR800 specifically accumulates in neuroblastoma. (a) Gamma decay of  $^{111}\text{In}$ - $\alpha\text{GD2}$ -IR800 is significantly higher in tumor than all other measured organs ( $p < 0.05$ ) except for spleen and liver. (b) Fluorescence intensity of  $^{111}\text{In}$ - $\alpha\text{GD2}$ -IR800 is higher in tumor than all organs at both timepoints ( $p < 0.005$ ). (c) Gamma and (d) optical biodistribution of  $^{111}\text{In}$ -isotype-IR800, shows tumor accumulation is significantly less than liver and spleen, with tumor-to-background ratios and differences dramatically lower than  $^{111}\text{In}$ - $\alpha\text{GD2}$ -IR800 at both timepoints

tracer injection (Fig. 3e; Supplementary Fig. 3d, 3e, and 4).

Tumors harvested from mice at days 4 and 6 ( $n=5$  from gamma biodistribution group) were also implanted in processed tissue cubes to evaluate the effect of tumor depth on gamma and fluorescent signal detection. Gamma decay signal was detected from the surface of 5 cm of processed tissue and increased as 5 mm slices were removed from the tissue cube (Fig. 3b, Supplementary Fig. 5). Gamma signal was detected through 5 cm of tissue when the probe was aimed directly at the tumor, but no signal was detected when the probe was angled away more than  $\sim 5$  degrees or moved laterally.

Fluorescence could not be visualized until only 5 mm of processed tissue covered the tumor.

The SPY-PHI camera also demonstrated efficacy in the detection of residual disease in and around the tumor bed after tumor resection. NB bearing mice ( $n=2$ ) were administered tracer 4 days prior to surgery, as prior biodistribution studies had demonstrated adequate TBR at that time. After laparotomy (Fig. 4a), complete tumor resection was attempted without IMI (Fig. 4b). Post-resection NIR imaging revealed residual fluorescence in the tumor bed, indicating likely residual disease (Fig. 4c) and was then used to remove the suspected residual disease (Fig. 4d; inset image of additionally resected tissue).

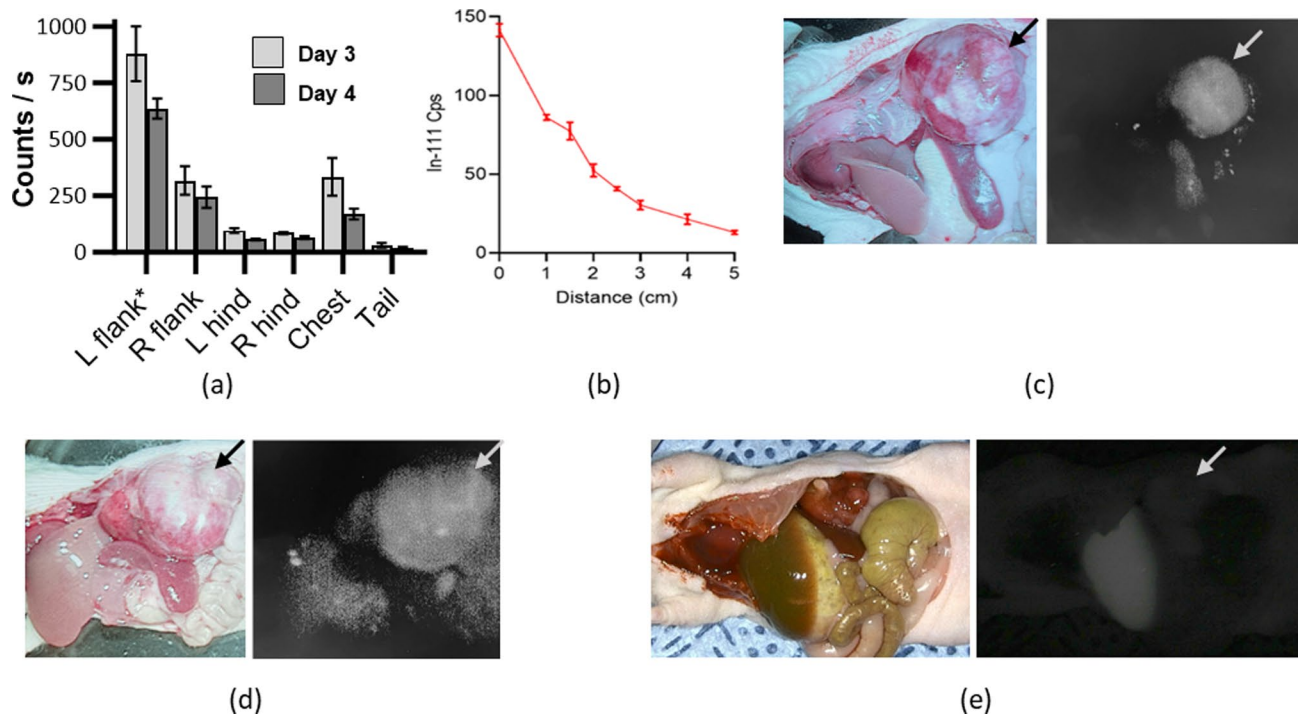


**Fig. 3** Handheld instruments can detect probe accumulation in the tumor. **(a)** Comparison of gamma decay of In-111 from different regions of the mouse body externally measured in situ with the handheld Neoprobe®, where the left flank contains the NB tumor and significantly greater decay ( $p < 0.0001$ ). **(b)** Gamma counts from excised tumor embedded in increasing thicknesses of processed tissue (0.072 MBq). **(c-d)** Representative images of neuroblastoma xenografts taken with SPY-PHI camera in white light (left) and NIR (right), 4 days after  $^{111}\text{In-}\alpha\text{GD2-IR800}$  injection and **(e)** 4 days after  $^{111}\text{In}$ -isotype-IR800 injection

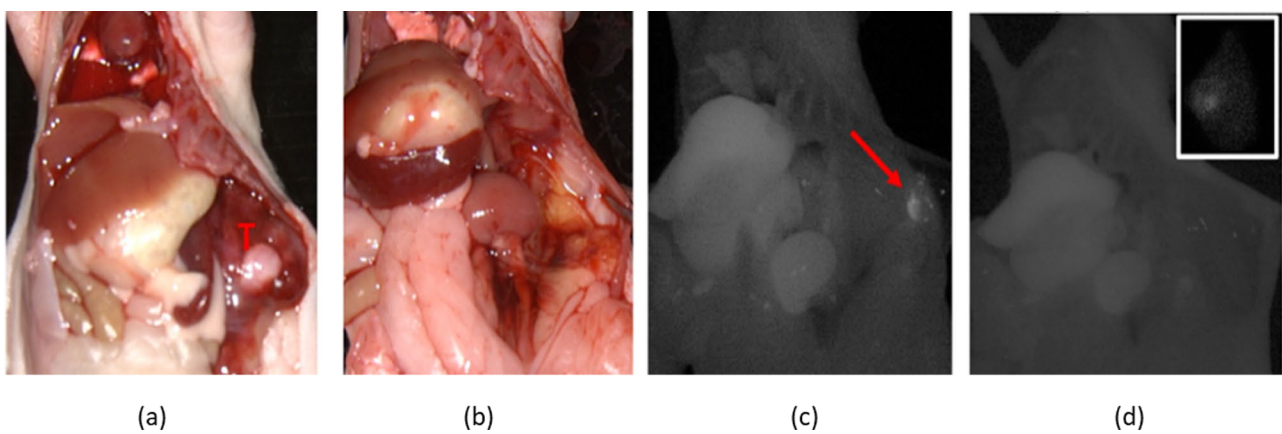


**Fig. 4** Fluorescence detection of residual tumor aids in complete resection. **(a)** Tumor is seen prior to attempted resection (white light; T denotes left adrenal tumor) while **(b)** no residual tumor was observed following resection. **(c)** Fluorescence imaging with the SPY-PHI camera demonstrated residual fluorescent tissue (arrow), which was then resected, **(d)** leaving no remaining fluorescent tissue in the tumor bed (inset: additionally resected fluorescent tissue)

**Discussion**

Multimodal therapy, including surgical resection, is crucial for the management of high-risk neuroblastoma (NB). Despite extensive therapy, 5-year survival remains only 40–50%, leading NB to be a disproportionately high cause of pediatric cancer mortality [2]. Incomplete macroscopic resection is associated with worse patient outcomes and maintenance immunotherapy is more

effective with less residual disease [6, 32–34]. Achieving an adequate degree of resection safely, however, is challenging, as these tumors are not well circumscribed, develop an intimate relationship with vital structures that must be preserved, and can form satellite lesions that are difficult to find. With only direct tumor visualization and palpation for guidance, up to 30% of resections for high-risk NB are inadequate, and up to 50% lead to

complications [6, 32, 34, 35]. IMI is an emerging strategy to specifically identify and visualize tumors, to facilitate a safer, more complete resection and thus, potentially improve post-operative outcomes, though it has not previously been used for pediatric cancer indications. In this study, we demonstrate the utility of our dual-labeled GD2-specific tracer to localize and visualize NB with commonly used intraoperative tools.

GD2 was selected as the IMI target because it is over-expressed in NB, as well as several other cancers, and has minimal expression on normal tissues. In fact, due to these features, the NIH has identified GD2 as one of the most critical tumor antigens for targeted therapies [5, 20–22, 36]. While radio-guided surgery (RGS) and fluorescence-guided surgery (FGS) have proven benefit, each technique has shortcomings overcome by the other [20, 37–39]. Consequently, we have chosen to dual-label our IMI agent, to enable detection of deeper or occult tumors (RGS) and tumor margin visualization (FGS). Therefore, DTPA- $\alpha$ GD2-IR800 was synthesized and radio-labeled with Indium-111 to evaluate it as an IMI agent in a mouse model of NB. While the binding affinity of DTPA- $\alpha$ GD2-IR800 is just under 10-fold lower than unlabeled antibody (21.31 nM versus 2.39 nM), it remains adequate for intraoperative imaging, based on other targeted antibody-based tracers [40]. The number of IRDye<sup>®</sup> 800CW and DTPA per molecule will also be adjusted in future work to optimize binding and signal. While tracer was tolerated well by all mice, pharmacology and toxicity studies must be conducted in the future.

Both gamma and fluorescence biodistributions demonstrated excellent antigen-specific accumulation of the tracer in tumor tissue, with some non-specific accumulation in the liver and spleen, as seen with other antibody-based IMI tracers. After 5 weeks of growth, the tumors used in these studies were an average of  $907.5 \pm 44.6$  mm<sup>3</sup> in volume ( $13.8 \pm 0.24$  mm in largest dimension). In gamma biodistribution studies, the tracer had excellent tumor accumulation ( $13.5 \pm 5.27\%$ ID/g on day 4 and  $5.58 \pm 0.48\%$ ID/g on day 6), tumor-to-blood ratios (3.9), and tumor-to-muscle ratios (30) (Fig. 2a). Similar results were seen in the fluorescence biodistribution, where the average fluorescence intensity of tumor ( $37.9 \pm 7.88$  AU/p<sup>2</sup> and  $16.8 \pm 4.30$  AU/p<sup>2</sup> on days 4 and 6) was significantly higher than all other measured organs on both days ( $p < 0.001$ ; Fig. 2b). Tumor-to-blood differences ( $31.1$  AU/p<sup>2</sup> on day 4 and  $16.37$  AU/p<sup>2</sup> on day 6) and tumor-to-muscle differences ( $33.3$  AU/p<sup>2</sup> on day 4 and  $16.0$  AU/p<sup>2</sup> on day 6) enabled excellent NIR fluorescence visualization of tumors. Fluorescence biodistribution was performed using the handheld SPY-PHI instrument, which is currently used clinically, rendering the results particularly relevant for surgical use of the tracer. Furthermore, the tumor was detectable in vivo with the Neoprobe<sup>®</sup> and

SPY-PHI NIR camera (Fig. 3), both widely available hand-held intraoperative instruments.

The isotope control tracer had very low tumor accumulation on both days ( $1.34 \pm 0.15\%$ ID/g and  $1.56 \pm 0.52\%$ ID/g) and was not significantly higher than any other organ (Fig. 2c). While fluorescence was higher in the tumor versus some background organs, it remained overall quite low ( $5.03 \pm 1.3$  AU/p<sup>2</sup> on day 4 and  $4.34 \pm 1.69$  AU/p<sup>2</sup> on day 6; Fig. 2d) and was significantly lower than the liver (Supplementary Fig. 3d, 3e, and 4). This indicates antigen-specific binding and accumulation of the anti-GD2 probe in the tumor, rather than accumulation due to the enhanced permeability and retention (EPR) effect.

To study IMI performance, the Neoprobe<sup>®</sup> and SPY-PHI tools were used in situ after tracer injection. Gamma decay detection with the handheld Neoprobe<sup>®</sup> was higher in the tumor-bearing left flank than in other body regions (Fig. 3a;  $p < 0.0001$ ) and strong qualitative fluorescence of the tumor was seen (Fig. 3c and d; Supplementary Fig. 3b and c). Furthermore, the effect of tumor depth on detection was assessed with a processed tissue phantom model. Using conventional surgical methods, identifying small tumors below a tissue or organ surface can prove extremely challenging. Gamma detection of the labeled tumor was excellent through up to 5 cm of intervening processed tissue (Fig. 3b). Gamma detection provided directional guidance, required by surgeons to continue dissection, as counts were highest when the probe was on an axis pointed directly towards the tumor. By comparison, fluorescence was significantly limited by depth, only visible through 5 mm or less of tissue, consistent with previously reported depth limitations of FGS [14, 15].

To further assess <sup>111</sup>In- $\alpha$ GD2-IR800-based IMI, mice with xenograft NB tumors were injected with the tracer and complete tumor resection was faithfully attempted without IMI guidance (standard surgery). Imaging with the SPY-PHI, however, revealed presumed residual disease that had not been appreciated during the initial white-light resection. The residual fluorescent tissue was then resected under IMI guidance (Fig. 4). Future work will include pathologic evaluation of the additional tissue resected by IMI guidance to further assess the specificity of the targeted tracer in vivo. We will also utilize our newly established rodent renal-sparing radical adrenalectomy survival surgery model, to compare safety, degree of resection, tumor recurrence, and survival following resection, with or without use of <sup>111</sup>In- $\alpha$ GD2-IR800-based IMI [41].

Overall, use of this probe in GD2-expressing cancer demonstrated an excellent tumor-to-background signal using intraoperative gamma and NIR hand-held detectors, enabling visualization and removal of suspected residual tumor tissue in mice with NB orthotopic

xenograft tumors. Other IMI tracers are limited in their use for resection of neuroblastoma. Wellens et al. previously generated an anti-GD2-IRDye800CW IMI tracer, which is fluorescent only and thus has a more limited depth of detection than the dual-labeled tracer [42]. Both our dual-labeled tracer and the Wellens fluorescent tracer have non-specific liver accumulation, which could limit the efficacy in detecting and visualizing liver metastases.

There are three currently FDA-approved fluorescent tracers for cancer (5-ALA, Cytalux or OTL38, and Luminex or LUM015), which similarly have limited depth of penetration. No dual-labeled tracers, which enable both fluorescence visualization, and radioactivity-based depth of detection are FDA-approved and those in clinical trials target carbonic anhydrase IX, gastrin-releasing peptide receptor, and CEA, which are not as uniformly and highly expressed in neuroblastoma [17, 19, 43, 44]. Collectively, our data demonstrate the potential to improve the safety and completeness of NB detection and resection using IMI with  $^{111}\text{In}$ - $\alpha\text{GD2}$ -IR800.

While the murine anti-GD2 antibody used in this study could be immunogenic in humans, it is an isotype variant of the FDA-approved chimeric antibody, Dinutuximab, which shares the same variable regions ( $V_H$  and  $V_L$ ) and thus establishes the utility of the anti-GD2 targeting strategy. We anticipate generating a similar agent with Dinutuximab which, even at higher doses and in combination with immunomodulatory drugs IL-2 and GM-CSF, is rarely immunogenic in humans [45]. The tracer will be further optimized for binding and fluorescence by adjusting the number of DTPA and IRDye<sup>®</sup> 800CW per antibody. Prior studies are encouraging that a single dose of Dinutuximab-based tracer for IMI, which is given without immunomodulatory agents and correlates with a human dose approximately 40% of the daily therapeutic dose, should have little effect on future therapy, though this will be important to confirm [46]. Because the mouse body is small relative to the size of the Neoprobe<sup>®</sup>, there may have been overlapping signal from the tumor, liver, and spleen *in situ*. Our orthotopic xenograft rat model should improve spatial separation of tumor and abdominal organs [46].

While there have been recent advances in tumor-specific antigen tracers in adult oncology, their utility in pediatric oncology remains limited [47, 48]. We have developed a functional IMI tracer that is detectable with excellent sensitivity and specificity by widely available surgical instruments. This novel IMI-based approach may facilitate safer and more complete resection of NB in children, with a potential survival benefit.

## Conclusions

We present a novel intraoperative imaging agent to enable safer and more complete operative resection by enhancing the targeted detection of tumor using tools already in regular clinical use. Our dual-labeled anti-GD2 tracer,  $^{111}\text{In}$ - $\alpha\text{GD2}$ -IR800, demonstrated antigen specificity and allowed specific detection and visualization of neuroblastoma in an animal model. This IMI tracer could provide a means to not only increase the completeness of resection, but also to minimize and potentially prevent surgical complications, thereby improving patient outcomes.

## Abbreviations

FGS	Fluorescent-guided surgery
IMI	Intraoperative molecular imaging
NB	Neuroblastoma
NIR	Near infrared
RGS	Radio-guided surgery
ROI	Regions of interest

## Supplementary Information

The online version contains supplementary material available at <https://doi.org/10.1186/s12967-024-05728-0>.

Supplementary Material 1

## Acknowledgements

Not applicable.

## Author contributions

LTR and RES contributed to the conceptualization, data curation, formal analysis, investigation, methodology, project administration, visualization, writing, and revising of this paper. RG and DG contributed to the conceptualization, investigation, visualization, and writing. DMM and SRV contributed to the data curation, conceptualization, investigation, visualization, and writing. PAB, MRR, APJ contributed to the investigation, analysis, and visualization. ACV, CTS, JDL, AGC, KED, IR, TKH, and JRN contributed to the investigation. LF contributed to the investigation and writing. GK, WBE, and MMM contributed to the conceptualization, funding acquisition, investigation, methodology, supervision, writing, and revising of this paper.

## Funding

This research was supported by University of Pittsburgh funds (GK); the RK Mellon Foundation Mellon Scholar Award (MMM); the Marjory K. Harmer endowment for Research in Pediatric Pathology (MMM); the NCI of the NIH (T32CA113263 - LTR, F32CA287961 - LTR, and R01 CA277664). This work utilized the Hillman Cancer Center In Vivo Imaging Facility, a shared resource at the University of Pittsburgh supported by NIH P30 CA047904 and the PAR-20-043, Cancer Center Support Grants (CCSGs). The content is solely the responsibility of the authors and does not necessarily represent the official views of the NIH. The funders had no role in study design, data collection and analysis, decision to publish, or preparation of the manuscript.

## Data availability

The datasets used and/or analyzed during the current study are available from the corresponding author on reasonable request.

## Declarations

### Ethics approval and consent to participate

Animal studies were performed in accordance with the protocols approved by the Institutional Animal Care and Use Committee of the University of Pittsburgh (IACUC protocol number: 19126346).

**Consent for publication**

Not applicable.

**Competing interests**

A patent has been submitted for <sup>111</sup>In-GD2-IR800 (application #63/382,434 for authors MMM, GK, WBE, and LTR).

**Author details**

<sup>1</sup>Department of General Surgery, University of Pittsburgh, 200 Lothrop Street, Pittsburgh, PA 15213, USA

<sup>2</sup>Department of Neurological Surgery, Children's Hospital of Pittsburgh of UPMC, 7131 Rangos Research Building, 530 45th Street, Pittsburgh, PA 15201, USA

<sup>3</sup>University of Pittsburgh School of Medicine, 3550 Terrace Street, Pittsburgh, PA 15213, USA

<sup>4</sup>Department of Biochemistry, University of Missouri, 117 Schweitzer Hall, Columbia, MO 65211, USA

<sup>5</sup>In Vivo Imaging Facility Core, Hillman Cancer Center, University of Pittsburgh Medical Center, 5115 Centre Avenue, Pittsburgh, PA 15232, USA

<sup>6</sup>Department of Immunology, University of Pittsburgh Medical Center, 200 Lothrop Street, Pittsburgh, PA 15213, USA

<sup>7</sup>Department of Pediatric General Surgery, University of Pittsburgh Medical Center, One Children's Hospital Drive, 4401 Penn Ave., Faculty Pavilion 7th Floor, Pittsburgh, PA 15224, USA

Received: 21 February 2024 / Accepted: 1 October 2024

Published online: 15 October 2024

**References**

- Siegel RL, Miller KD, Fuchs HE, Jemal A, Cancer Statistics. 2021. *CA Cancer J Clin.* 2021;71(1):7–33. Epub 2021/01/13. doi: 10.3322/caac.21654. PubMed PMID: 33433946.
- Cohn SL, Pearson ADJ, London WB, et al. The International Neuroblastoma Risk Group (INRG) classification system: an INRG Task Force Report. *J Clin Oncol.* 2009;27(2):289–97. <https://doi.org/10.1200/JCO.2008.16.6785>.
- Gatta G, Botta L, Rossi S, et al. Childhood cancer survival in Europe 1999–2007: results of EUROCare-5—a population-based study. *Lancet Oncol.* 2014;15(1):35–47. [https://doi.org/10.1016/S1470-2045\(13\)70548-5](https://doi.org/10.1016/S1470-2045(13)70548-5).
- Tas ML, Reedijk AMJ, Karim-Kos HE, et al. Neuroblastoma between 1990 and 2014 in the Netherlands: increased incidence and improved survival of high-risk neuroblastoma. *Eur J Cancer.* 2020;124:47–55. <https://doi.org/10.1016/j.ejca.2019.09.025>.
- Sait S, Modak S. Anti-GD2 immunotherapy for neuroblastoma. *Expert Rev Anticancer Ther.* 2017;17(10):889–904. <https://doi.org/10.1080/14737140.2017.1364995>.
- Cañete A, Jovani C, Lopez A, Costa E, Segarra V, Fernández JM, et al. Surgical treatment for neuroblastoma: complications during 15 years' experience. *J Pediatr Surg.* 1998;33:1526–30.
- Holmes K, Pötschger U, Pearson ADJ, Sarnacki S, Cecchetto G, Gomez-Chacon J, et al. Influence of surgical excision on the survival of patients with stage 4 high-risk neuroblastoma: a report from the HR-NBL1/SIOPEN study. *J Clin Oncol.* 2020;38:2902–15.
- von Allmen D, Davidoff AM, London WB, Van Ryn C, Haas-Kogan DA, Kreissman SG, et al. Impact of extent of resection on Local Control and survival in patients from the COG A3973 study with high-risk neuroblastoma. *J Clin Oncol.* 2017;35:208–16.
- Morton DL, Wen D-R, Wong JH, Economou JS, Cagle LA, Storm FK, et al. Technical Details of Intraoperative Lymphatic Mapping for Early Stage Melanoma. *Arch Surg.* 1992;127:392–9.
- Wang Z, Wu L-C, Chen J-Q. Sentinel lymph node biopsy compared with axillary lymph node dissection in early breast cancer: a meta-analysis. *Breast Cancer Res Treat.* 2011;129:675–89.
- Van Oosterom MN, Rietbergen DDD, Welling MM, Van Der Poel HG, Maurer T, Van Leeuwen FWB. Recent advances in nuclear and hybrid detection modalities for image-guided surgery. *Expert Rev Med Dev.* 2019;16(8):711–34. <https://doi.org/10.1080/17434440.2019.1642104>.
- Commissioner O of the. FDA Approves New Imaging Drug to Help Identify Ovarian Cancer Lesions [Internet]. FDA. FDA. 2021 [cited 2023 Mar 29]. <https://www.fda.gov/news-events/press-announcements/fda-approves-new-imaging-drug-help-identify-ovarian-cancer-lesions>
- Tanyi JL, Randall LM, Chambers SK, Butler KA, Winer IS, Langstraat CL et al. A phase III study of pafolacianine injection (OTL38) for intraoperative imaging of Folate receptor–positive ovarian Cancer (study 006). *J Clin Oncol.* 2023;41(2):276–84.
- Boogerd LSF, Hoogstins CES, Schaap DP, et al. Safety and effectiveness of SGM-101, a fluorescent antibody targeting carcinoembryonic antigen, for intraoperative detection of colorectal cancer: a dose-escalation pilot study. *Lancet Gastroenterol Hepatol.* 2018;3(3):181–91. [https://doi.org/10.1016/S2468-1253\(17\)30395-3](https://doi.org/10.1016/S2468-1253(17)30395-3).
- Gao RW, Teraphongphom NT, van den Berg NS, et al. Determination of Tumor margins with Surgical Specimen Mapping using Near-Infrared fluorescence. *Cancer Res.* 2018;78(17):5144–54. <https://doi.org/10.1158/0008-5472.CAN-18-0878>.
- Gangadharan S, Sarkaria IN, Rice D, Murthy S, Braun J, Kucharczuk J, et al. Multinstitutional Phase 2 Clinical Trial of Intraoperative Molecular Imaging of Lung Cancer. *Ann Thorac Surg.* 2021;112:1150–9.
- Hekman MC, Rijpkema M, Muselaers CH, Oosterwijk E, Hulsbergen-Van de Kaa CA, Boerman OC, et al. Tumor-targeted dual-modality imaging to improve intraoperative visualization of Clear Cell Renal Cell Carcinoma: A First in Man Study. *Theranostics.* 2018;8:2161–70.
- Hekman MCH, Rijpkema M, Bos DL, Oosterwijk E, Goldenberg DM, Mulders PFA, et al. Detection of Micrometastases using SPECT/Fluorescence dual-modality imaging in a CEA-Expressing Tumor Model. *J Nucl Med.* 2017;58:706–10.
- Vargas SH, Ghosh SC, Azhdarinia A. New Developments in Dual-labeled Molecular Imaging agents. *J Nucl Med.* 2019;60:459–65.
- Straathof K, Flutter B, Wallace R, et al. Antitumor activity without on-target off-tumor toxicity of GD2–chimeric antigen receptor T cells in patients with neuroblastoma. *Sci Transl Med.* 2020;12(571):eabd6169. <https://doi.org/10.1126/scitranslmed.abd6169>.
- Butch ER, Mead PE, Amador Diaz V, et al. Positron Emission Tomography detects in vivo expression of Disialoganglioside GD2 in Mouse models of primary and metastatic osteosarcoma. *Cancer Res.* 2019;79(12):3112–24. <https://doi.org/10.1158/0008-5472.CAN-18-3340>.
- Lammie G, Cheung N, Gerald W, Rosenblum M, Cordoncardo C, GANGLIOSIDE GD(2) EXPRESSION IN THE HUMAN NERVOUS-SYSTEM AND IN NEUROBLASTOMAS - AN IMMUNOHISTOCHEMICAL STUDY. *Int J Oncol.* 1993;3(5):909–15. <https://doi.org/10.3892/ijo.3.5.909>.
- Rinehardt HN, Longo S, Gilbert R, et al. Handheld PET probe for Pediatric Cancer surgery. *Cancers.* 2022;14(9):2221. <https://doi.org/10.3390/cancers14092221>.
- Ovacik M, Lin K. Tutorial on monoclonal antibody pharmacokinetics and its considerations in Early Development. *Clin Transl Sci.* 2018;11(6):540–52. <https://doi.org/10.1111/cts.12567>.
- Croce AC, Bottiroli G. Autofluorescence spectroscopy and imaging: a Tool for Biomedical Research and diagnosis. *Eur J Histochem EJH.* 2014;58:2461.
- Gao RW, Teraphongphom NT, van den Berg NS, Martin BA, Oberhelman NJ, Divi V, et al. Determination of Tumor margins with Surgical Specimen Mapping using Near-Infrared fluorescence. *Cancer Res.* 2018;78:5144–54.
- Nalla A, Buch I, Hesse B. Easy and efficient <sup>111</sup>Indium labeling of long-term stored DTPA conjugated protein. *Curr Radiopharmaceuticals.* 2011;4(1):1–4.
- Vävere AL, Butch ER, Dearling JL, et al. <sup>64</sup>Cu-p-NH<sub>2</sub>-Bn-DOTA-hu14.18K322A, a PET Radiotracer Targeting Neuroblastoma and Melanoma. *J Nucl Med.* 2012;53(11):1772–8. <https://doi.org/10.2967/jnumed.112.104208>.
- Nguyen F, Guan P, Guerrero DT, et al. Structural optimization and enhanced prodrug-mediated delivery overcomes Camptothecin Resistance in High-Risk Solid tumors. *Cancer Res.* 2020;80(19):4258–65. <https://doi.org/10.1158/0008-5472.CAN-20-1344>.
- Nigam S, McCarl L, Kumar R, Edinger RS, Kurland BF, Anderson CJ, et al. Preclinical ImmunoPET imaging of Glioblastoma-infiltrating myeloid cells using Zirconium-89 labeled Anti-CD11b antibody. *Mol Imaging Biol.* 2020;22:685–94.
- Nguyen F, Guan P, Guerrero DT, Kolla V, Naraparaju K, Perry LM, et al. Structural optimization and enhanced prodrug-mediated delivery overcomes Camptothecin Resistance in High-Risk Solid tumors. *Cancer Res.* 2020;80:4258–65.
- Holmes K, Pötschger U, Pearson ADJ, et al. Influence of surgical excision on the survival of patients with stage 4 high-risk neuroblastoma: a report from the HR-NBL1/SIOPEN study. *J Clin Oncol.* 2020;38(25):2902–15. <https://doi.org/10.1200/JCO.19.03117>.

33. Yu AL, Uttenreuther-Fischer MM, Huang CS, et al. Phase I trial of a human-mouse chimeric anti-disialoganglioside monoclonal antibody ch14.18 in patients with refractory neuroblastoma and osteosarcoma. *J Clin Oncol.* 1998;16(6):2169–80. <https://doi.org/10.1200/jco.1998.16.6.2169>.
34. von Allmen D, Davidoff AM, London WB, et al. Impact of extent of resection on Local Control and survival in patients from the COG A3973 study with high-risk neuroblastoma. *J Clin Oncol.* 2017;35(2):208–16. <https://doi.org/10.1200/JCO.2016.67.2642>.
35. Cañete A, Jovani C, Lopez A, et al. Surgical treatment for neuroblastoma: complications during 15 years' experience. *J Pediatr Surg.* 1998;33(10):1526–30. [https://doi.org/10.1016/S0022-3468\(98\)90490-0](https://doi.org/10.1016/S0022-3468(98)90490-0).
36. Cheever MA, Allison JP, Ferris AS, et al. The prioritization of Cancer antigens: a National Cancer Institute Pilot Project for the Acceleration of Translational Research. *Clin Cancer Res.* 2009;15(17):5323–37. <https://doi.org/10.1158/1078-0432.CCR-09-0737>.
37. Wang Z, Wu LC, Chen JQ. Sentinel lymph node biopsy compared with axillary lymph node dissection in early breast cancer: a meta-analysis. *Breast Cancer Res Treat.* 2011;129(3):675–89. <https://doi.org/10.1007/s10549-011-1665-1>.
38. Hernot S, van Manen L, Debie P, Mieog JSD, Vahrmeijer AL. Latest developments in molecular tracers for fluorescence image-guided cancer surgery. *Lancet Oncol.* 2019;20(7):e354–67. [https://doi.org/10.1016/S1470-2045\(19\)30317-1](https://doi.org/10.1016/S1470-2045(19)30317-1).
39. Vahrmeijer AL, Hutteman M, van der Vorst JR, van de Velde CJH, Frangioni JV. Image-guided cancer surgery using near-infrared fluorescence. *Nat Rev Clin Oncol.* 2013;10(9):507–18. <https://doi.org/10.1038/nrclinonc.2013.123>.
40. Rudnick SI, Lou J, Shaller CC, Tang Y, Klein-Szanto AJP, Weiner LM, et al. Influence of Affinity and Antigen internalization on the Uptake and Penetration of Anti-HER2 antibodies in solid tumors. *Cancer Res.* 2011;71:2250–9.
41. Sever RE, Rosenblum LT, Reyes-Múgica M, Edwards WB, Malek MM, Kohanbash G. Survival following complete resection of neuroblastoma in novel orthotopic rat xenograft model. *Sci Rep.* 2023;13:20214.
42. Wellens LM, Deken MM, Sier CFM, Johnson HR, de la Jara Ortiz F, Bhairosingh SS, et al. Anti-GD2-IRDye800CW as a targeted probe for fluorescence-guided surgery in neuroblastoma. *Sci Rep.* 2020;10:17667.
43. Ameis HM, Drenckhan A, Freytag M, Izbicki JR, Supuran CT, Reinschagen K, et al. Carbonic anhydrase IX correlates with survival and is a potential therapeutic target for neuroblastoma. *J Enzyme Inhib Med Chem.* 2016;31:404–9.
44. Kim S, Hu W, Kelly D, Hellmich M, Evers M, Chung DH. Gastrin-releasing peptide is a growth factor for human neuroblastomas. *Ann Surg.* 2002;235:621–30.
45. Yu AL, Gilman AL, Ozkaynak MF, et al. Long-term follow-up of a phase III study of ch14.18 (Dinutuximab) + cytokine immunotherapy in children with high-risk neuroblastoma: COG study ANBL0032. *Clin Cancer Res.* 2021;27(8):2179–89. <https://doi.org/10.1158/1078-0432.CCR-20-3909>.
46. Wellens LM, Deken MM, Sier CFM, et al. Anti-GD2-IRDye800CW as a targeted probe for fluorescence-guided surgery in neuroblastoma. *Sci Rep.* 2020;10(1):17667. <https://doi.org/10.1038/s41598-020-74464-4>.
47. Hernot S, van Manen L, Debie P, Mieog JSD, Vahrmeijer AL. Latest developments in molecular tracers for fluorescence image-guided cancer surgery. *Lancet Oncol.* 2019;20:e354–67.
48. Vahrmeijer AL, Hutteman M, van der Vorst JR, van de Velde CJH, Frangioni JV. Image-guided cancer surgery using near-infrared fluorescence. *Nat Rev Clin Oncol.* 2013;10:507–18.

### Publisher's note

Springer Nature remains neutral with regard to jurisdictional claims in published maps and institutional affiliations.